Polarimetric performance of Si/CdTe semiconductor Compton camera

Shin'ichiro Takeda [a], Hirokazu Odaka [a,b], Junichiro Katsuta [a,b], Shin-nosuke Ishikawa [a,b], So-ichiro Sugimoto [a,b], Yuu Koseki [a], Shin Watanabe [a,b], Goro Sato [a], Motohide Kokubun [a], Tadayuki Takahashi [a,b], Kazuhiro Nakazawa [b], Yasushi Fukazawa [c], Hiroyasu Tajima [d], Hidenori Toyokawa [e]

[a] *Institute of Space and Astronautical Science, 3-1-1, Yoshinodai Sagamihara 229-8510, Japan*
[b] *University of Tokyo, 7-3-1, Hongo, Bunkyo, Tokyo 113-0033, Japan*
[c] *Hiroshima University, 1-3-1, Kagamiyama, Higashi-Hiroshima 739-8526,Japan*
[d] *Kavli Institute for Particle Astrophysics and Cosmology, Stanford University, Stanford, CA 94309-4349, USA*
[e] *Japan Synchrotron Radiation Research Institute, 1-1-1, Kouto, Sayo-cho, Sayo-gun, Hyogo 679-5198, Japan*

Abstract

A Compton camera has been developed based on Si and CdTe semiconductor detectors with high spatial and spectral resolution for hard X-ray and γ-ray astrophysics applications. A semiconductor Compton camera is also an excellent polarimeter due to its capability to precisely measure the Compton scattering azimuth angle, which is modulated by linear polarization. We assembled a prototype Compton camera and conducted a beam test using nearly 100% linearly polarized γ-rays at SPring-8.

Key words: Gamma-ray astronomy, Compton camera, Polarimeter

1. Introduction

Existing γ-ray observatories were designed to make precise measurements of the energy spectrum, intensity distribution and time variability of cosmic γ rays. However, for many sources, we have not yet reached a clear understanding of the energy transport system which leads to non-thermal emission in the strong gravitational field or magnetic field around black hole candidates, neutron stars or jet-dominant active galactic nuclei. Gamma-ray polarization properties, which have rarely been studied, would provide a new test of the various emission models. Photons emitted by Compton scattering in an accretion disk or generated by synchrotron radiation in a magnetic field will be polarized, and will, therefore, carry a lot of information on the geometry of magnetic and radiation fields near to the central engines [1–3]. In next generation observatories, polarization measurements are expected to be a powerful method of probing high-energy emission mechanisms.

Recently, new polarimeters utilizing the Compton scattering process inside the detectors have been proposed [4–6] for astrophysics in the hard X-ray or γ-ray band (10 keV–MeV). We expect a relatively large polarization ($\sim$10%) in this energy band where non-thermal emissions from celestial objects are dominant. In contrast, imaging gas polarimeters utilizing the photo-absorption process [7] suffer from the small polarization ($<$1%) in the soft X-ray band

Email address: takeda@astro.isas.jaxa.jp (Shin'ichiro Takeda).

(up to 10 keV) where thermal emissions are dominant. Measurements of small polarization require great care for systematic effects in polarization signals. One drawback in the hard X-ray or γ-ray band is the weakness of signals from celestial objects compared to those in the X-ray band while background environment is not better due to those induced by charged particles in orbit. To realize a hard X-ray or γ-ray polarimeter without sacrificing detection efficiency it is essential to take advantage of the background reduction capabilities provided by Compton kinematics.

We have previously proposed a novel semiconductor Compton camera [8,9] based on advanced technologies for Si and CdTe imaging devices which we have accumulated over the past 10 years. Deposit energies and interaction positions are precisely measured thanks to the fine energy resolution (ΔE/E$\sim$1%) and position resolution (<1 mm) of semiconductor detectors. These provide strict constraints on event topologies and energetics of Compton kinematics for all events recorded in the detectors. We can utilize the incident direction of the γ-rays inferred from the Compton kinematics to distinguish target signals from the background. In our previous work [10,11], we developed prototype Compton cameras and verified their performance by comparing experimental data with Monte Carlo (MC) simulations. In this verification process, we successfully obtained γ-ray images of point sources from 60 to 662 keV using Compton kinematics. We also successfully demonstrated the capability of imaging extended sources [12]. The typical resolution of the scattering angle (Angular Resolution Measure or ARM) was 3.5° (FWHM) and 2.5° (FWHM) at 356 keV and 511 keV, respectively. These resolutions are close to the theoretical limit imposed by Doppler broadening [13].

Our camera is also sensitive to the polarization of incident photons since the azimuth angle of Compton scattering is modulated by the polarization. The high position resolution realized by semiconductor devices provides an excellent means of measuring the modulation of the azimuth scattering angle [14,15]. In this paper, we describe the capability of a prototype semiconductor Compton camera to measure polarization phase and magnitude. This capability was demonstrated using polarized γ-rays at SPring-8 [16]. In Section 3 we describe the detector setup. In order to account for instrumental effects, we conducted a MC simulation that included detailed detector geometries and charge transport in the detectors. Section 4 contains a comparison of the experimental and simulation results for basic detector properties. In Sections 5 and 6 we describe the beam line setup and the beam test results, respectively. Finally, in Section 7 we discuss the polarimetric performance of the Soft Gamma-ray Detector (SGD) [17] for the ASTRO-H mission [18,19], previously known as the NeXT mission– the 6th Japanese X-ray satellite that is scheduled for launch in 2014.

2. Measurement of the Degree and Direction of Polarization

According to the Klein-Nishina formula, the Compton scattering cross section per electron for a linearly polarized γ-ray is expressed as:

$$\frac{d\sigma}{d\Omega} = \frac{r_e^2}{2}\left(\frac{E'}{E_0}\right)^2\left(\frac{E'}{E_0} + \frac{E_0}{E'} - 2\sin^2\theta\cos^2\eta\right) \quad (1)$$

where, r_e denotes the classical electron radius, E_0 the energy of the incident γ-ray, E' the scattered γ-ray, θ the polar angle of Compton scattering, and η the azimuth scattering angle with respect to the electric vector of the incident photon. This relationship can be used to deduce the polarization parameters from the azimuthal angle distribution observed in the detector.

Here, we define the experimental azimuthal angle distribution as $N_{\rm obs}(\phi)$, which includes the effect of instrument responses. Some experiments rotate the entire detector system in order to reduce the effect of azimuthal angle dependence of the detector response. Since rotating the detector system imposes technical complexities on the detector system, we took an alternative approach here. We made corrections for the detector response as obtained by MC simulations. The corrected azimuthal angle distribution or $N_{\rm cor}(\phi)$ is defined as:

$$N_{\rm cor}(\phi) = \frac{N_{\rm obs}(\phi)}{R(\phi)} \quad (2)$$

in which,

$$R(\phi) = \frac{N_{\rm iso}(\phi)}{\overline{N_{\rm iso}}} \quad (3)$$

where, $N_{\rm iso}(\phi)$ denotes the azimuthal angle distribution for non-polarized γ-rays, which can be derived from simulations or measured experimentally, and $\overline{N_{\rm iso}}$ the average value per bin. We need to use simulated $N_{\rm iso}(\phi)$ since it is not practical to measure $N_{\rm iso}(\phi)$ experimentally for all energy points in

our energy band. Section 4 describes the MC simulator developed for the Compton camera, and Section 6 includes the verification of the simulated $N_{\rm iso}(\phi)$ and conducting experiments.

The polarimetric information of incident γ-rays is derived by fitting $N_{\rm cor}(\phi)$ using the theoretical function of [20]:

$$N_{\rm cor}(\phi) = A\left(1 + Q\cos 2\left(\phi - \phi_0 - \frac{\pi}{2}\right)\right) \quad (4)$$

where, A denotes an average of the distribution, ϕ_0 the direction of the polarization vector, and Q the modulation factor proportional to the degree of polarization. Q can also be expressed as:

$$Q = \frac{N_{\rm cor,max} - N_{\rm cor,min}}{N_{\rm cor,max} + N_{\rm cor,min}} \quad (5)$$

Thus, the degree of polarization can be given by:

$$\Pi = \frac{Q}{Q_{100}} \quad (6)$$

where, Q_{100} denotes the modulation factor for 100% linearly polarized γ rays. Q_{100} is known as the analyzing power of the instrument and must be determined through experiments or simulations.

3. Polarimetric System

In order to validate MC simulation and the resulting instrument response function, and demonstrate the polarimetric performance of a semiconductor Compton camera, we conducted a beam test using nearly 100% polarized γ-rays with high brilliance at SPring-8. A prototype semiconductor Compton camera was assembled for the beam test in a configuration affording maximum analyzing power. As shown in Equation 1, the modulation of the azimuth scattering angle is maximized at a polar scattering angle of around 90°. Therefore, the horizontal direction of the scattering photons should be covered for sensitive measurements.

Figure 1 shows a 3D view and cross-sectional view of the detector configuration used for the Compton camera. A low-noise DSSD (Double-sided Silicon Strip Detector) [21–23] functions as a scatterer, while the CdTe pixel detectors [24,25] function as absorbers. Table 1 summarizes the dimensions and typical performance of each DSSD and CdTe detector element. A stacked CdTe module consisting of four layers of CdTe pixel detectors is placed 14.5 mm under the DSSD. Each CdTe layer contains four

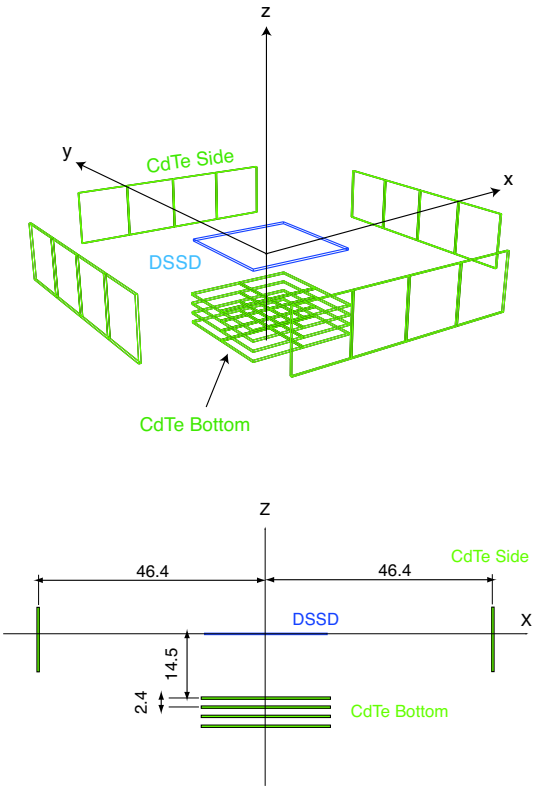

Fig. 1. A three-dimensional view (top) and a cross-sectional view in the z–x plane (bottom) of detector setup for the beam test.

CdTe detectors in a 2×2 arrangement. We symmetrically covered the horizontal direction of the DSSD with four CdTe side modules to improve this system's analyzing power. Four CdTe pixel detectors are used in each CdTe side module. The side CdTe detectors cover the scattering angle of 80° to 105° for γ-rays incoming along the Z-axis.

Figure 2 shows a schematic diagram of the Compton camera read-out system. Thirty-four front-end VA64TA ASICs [26] are used to read-out 2176 detector channels. The FPGAs (Field Programmable Gate Arrays) in the "CdTe readout box" and "DSSD readout box" control these ASICs. Each Readout Box is controlled by a dedicated "SpaceWire digital I/O board", where triggers from the detectors are processed and the read-out sequence is managed. The entire system is managed by a small computer–SpaceCube (SpC) [27]. The system is based on the SpaceWire interface standard adopted for the next generation of major satellite experiments.

Detector	Active Area [mm]	Thickness [mm]	Strip Pitch (Pad Size) [mm]	Bias [V]	Energy Resolution
DSSD (Si)	25.6 × 25.6	0.5	0.4	250	1.6 keV (FWHM) at 59.5 keV
CdTe pixel	13.2 × 13.2	0.5	1.35	600	2.0 keV (FWHM) at 81 keV
					ΔE/E ∼1 % (FWHM) at 511 keV

Table 1
Dimensions, operating bias voltages, energy resolutions for DSSD and CdTe detectors.

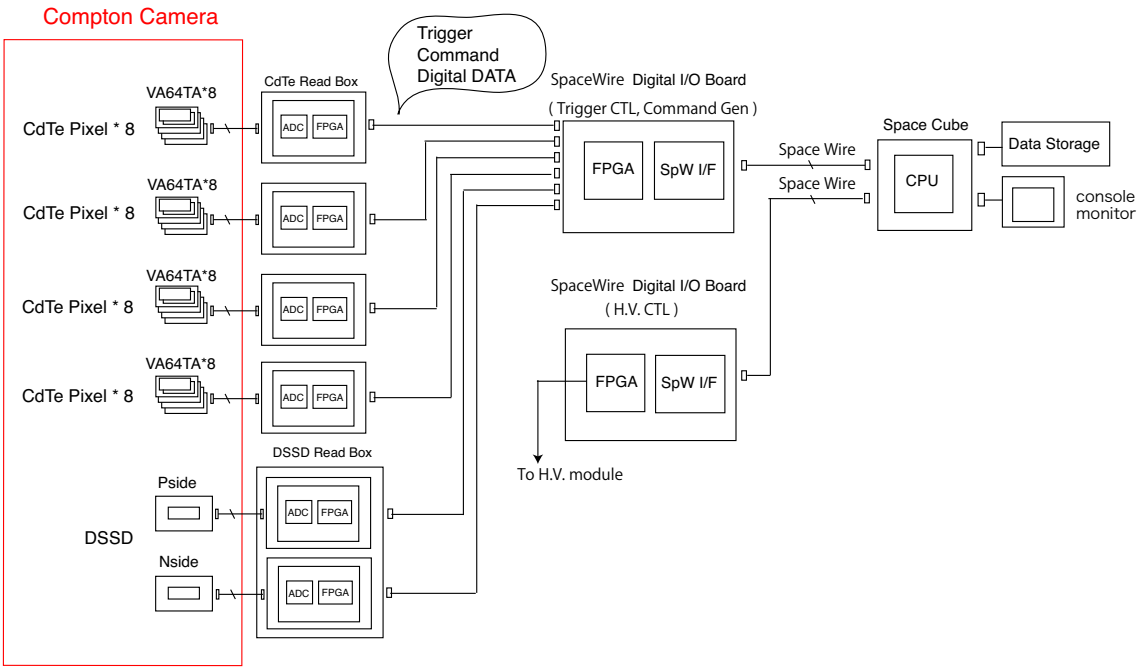

Fig. 2. Schematic diagram of Compton camera readout system

4. Monte Carlo Simulator

The systematic uncertainties of the instruments ultimately limit polarimetric sensitivity. In our case, the accuracy of MC simulation of the detector response to non-polarized γ-rays is the key (see Section 2).

The simulator was developed based on the Geant4 toolkit. In order to account for physical processes caused by the polarized γ-rays including the Doppler broadening effect, we employed the latest version (Geant4.9.2). In order to convert the energy deposits simulated by Geant4 into actual energy measured in real devices, we take into account the physical processes not simulated by Geant4, such as the thermal diffusion of electrons and holes in semiconductor devices, and charge collection efficiency dependent on the initial position in a given device. We also added Gaussian noise to each detector segment to correctly simulate the measured energy resolution.

4.1. *DSSD response*

The initial charge cloud size and thermal diffusion depending on the depth of the charge from the charge collection surface (i.e., readout strips) determine the amount of charge sharing between adjacent detector segments as reported in our experimental study [22]. In this previous work, we found "dead spots" under the SiO_2 layer between the p-strips due to the local potential minimum. This effect is not implemented since the contribution is on the order of 0.1%.

The size and shape of initial electron-hole clouds are simulated by using the electron tracking code included in the Geant4 library. In this process we consider multi scattering, ionization, and bremsstrahlung radiation. Thermal diffusion is implemented in order to reproduce the experimental multiplicity of detector hits and the energy distribution in charge sharing for 59.5 keV and 122 keV

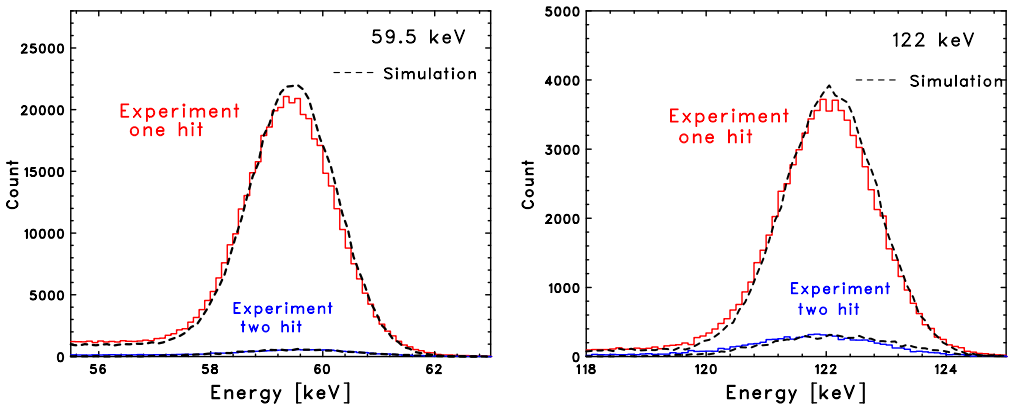

(a) (b)

Fig. 3. Comparison of DSSD spectrum between experiment and simulator output (Left: 59.5 keV; Right: 122 keV). Note that we used absolute normalization, given the intensity of the source and the measured dead time.

γ rays.

Figure 3 compares the experimental spectra with the simulation results for 59.5 keV and 122 keV γ rays. The spectra for one-hit events (hit in a single strip) and two-hit events (hits in two adjacent strips) are shown together with the simulation spectra indicated by dotted lines. Note that we used absolute normalization for the simulated spectra, given the intensity of the source and the measured dead time. The spectra are well reproduced within the 5% level. This suggests that DSSD detector response is properly implemented in the simulator.

4.2. *CdTe pixel response*

Unlike silicon devices, CdTe devices have slow mobility and a short lifetime for holes, and therefore require careful treatment of the charge trapping in simulation. We employed the weighting potential based on the Shockley-Ramo theorem [28,29]. In this method, the 3-dimensional position dependence of the charge collection efficiency is calculated using the 3-dimensional weighting potential and mean free path of a charge. The mean free path is characterized by the product of mobility (μ) and lifetime (τ) of a charge and the internal electric field as:

$$\lambda_e = (\mu\tau)_e E, \quad \lambda_h = (\mu\tau)_h E$$

Our approach described here does not take into account some widely known effects such as nonuniform strength of the electric field in Shottoky CdTe devices [30,31] and the polarization effect. The effect of a nonuniform electric field has yet to be established and therefore not implemented in the simulation. The polarization effect is negligible under a high electric field and at low temperature (600 V, -20°C) in this study. We used the $\mu\tau$ product values of 5×10^{-3} cm^2/V and 1.5×10^{-4} cm^2/V for electrons and holes, respectively, as obtained by applying the "$\mu\tau$-model" spectral fit method to the 4×4 mm, planar-type CdTe detector with a thickness of 0.5 mm. Our group developed the "$\mu\tau$-model" fit method and applied it to a response study for a total of 32,000 CdZnTe detectors [32] in the BAT instrument onboard the Swift satellite. In this method, we fit the spectral shape to extract parameters $(\mu\tau)_e$ and $(\mu\tau)_h$ by utilizing the fact that $(\mu\tau)_e$ is sensitive to the peak position in a spectrum, while $(\mu\tau)_h$ determines the amount of the tail component. A detailed description of this method is given in [33].

The typical charge collection time in CdTe devices is a few hundred nanoseconds; therefore, the spread of the hole cloud due to thermal diffusion could be estimated on the order of 10 μm. Although this parameter depends on the depth of interaction within the device, we simply extracted the average value and implemented it in the simulator so as to reproduce the hit multiplicity and energy distribution in charge-sharing events by using the experimental data for 59.5 keV, 122 keV and 511 keV γ rays.

Figure 4 presents the experimental spectra for single hit events together with the simulation spectra with different degrees of detector response effects. Absolute normalization is applied to the simulation spectra. Three simulation spectra with the following detector response effects are shown to illustrate those effects on the final spectra: (a) no charge trap-

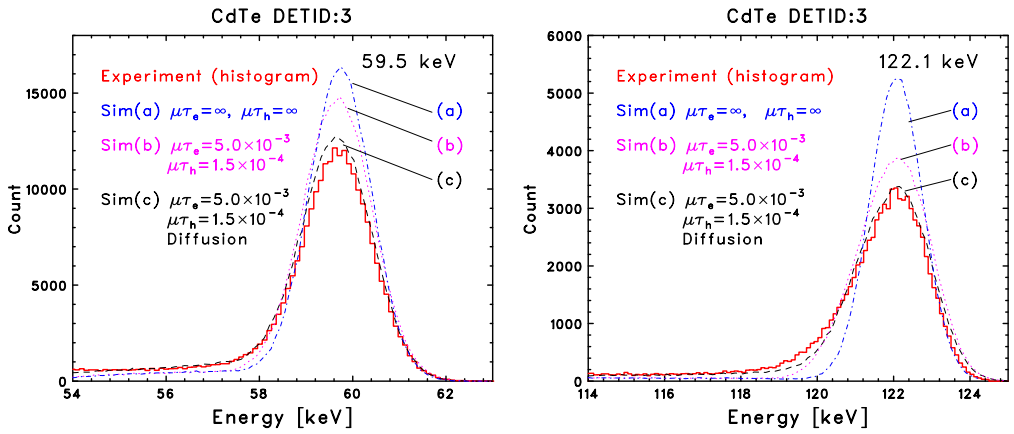

(a) (b)

Fig. 4. Comparison of CdTe spectrum between experiment and simulator output. (See the text for details.)

ping or diffusion effect, (b) charge trapping effect included with no diffusion effect, and (c) both charge trapping and diffusion effects included.

The differences between cases (a) and (b) are the increased tail structure and reduced peak in the spectrum as a result of charge trapping due to low $\mu\tau$ values. In case (c), the energy deposits near the pixel boundary are shared by adjacent pixels, thereby reducing the number of single hit events and losing the small fraction of shared charge below the energy threshold, which contribute to the increased tail. The experimental spectrum is reasonably reproduced when including both trapping and diffusion effects.

5. Experimental Setup

We conducted the experiment at High Energy Inelastic Scattering Beamline BL08W of SPring-8 from October 23 to 25, 2008. Figure 5 shows a schematic view of our experimental setup. The incident beam energy was 250 keV with beam intensity of 2×10^{10} photons/s. In order to reduce the beam intensity, we used photons scattered horizontally in the beam direction within an aluminum block placed at the beam line. The intensity incoming our detector system was 1.8×10^{5} photons/s. As shown in this schematic view, the Compton camera is shielded by Pb so that the detector can only view photons with a scattering angle of 90±1.5°. The circular region with a diameter of 30 mm on the DSSD surface was illuminated by the polarized beam. The resulting energy was 168±1.4 keV, with a 92.5±0.3% degree of polarization in the incoming photons.

In order to study systematic effects associated with the direction of the polarization vector, the data was taken at various incident polarization vector angles by rotating the Compton camera itself. As shown in Fig. 5, we rotated the Compton camera for seven polarization vector angles at 0°, 15°, 22.5°, 30°, 45°, 90° and 180° relative to the Compton camera coordinates and with rotation angle accuracy of about 0.2 to 0.3°.

6. Analysis and Results

We used the coincidence events recorded in the DSSD and CdTe side detectors. Figure 6(a) shows the 2-dimensional scatter plot of energy deposited in the DSSD and CdTe side detectors. The peak around the Si energy deposit of about 40 keV and CdTe energy deposit of about 130 keV should correspond to events where incident 168 keV γ-rays are scattered in the DSSD in the horizontal direction, and then fully absorbed in the CdTe side detectors. We selected events that satisfy 165 keV $< E_{\rm Si} + E_{\rm CdTe} <$ 175 keV and 35 keV$< E_{\rm Si} <$ 50 keV (i.e., region enclosed by straight lines in the scatter plot of Fig. 6(a)). Figure 6(b) shows the ARM distributions; the dotted line indicates that of all events, with the solid line indicating that of events selected in the scatter plot of Fig. 6(a). This selection drastically suppressed the events with Compton cones set apart from the beam direction.

The azimuth scattering angle was derived from energy deposit positions in the DSSD and CdTe detectors. The top panel of Fig. 7 shows the azimuth

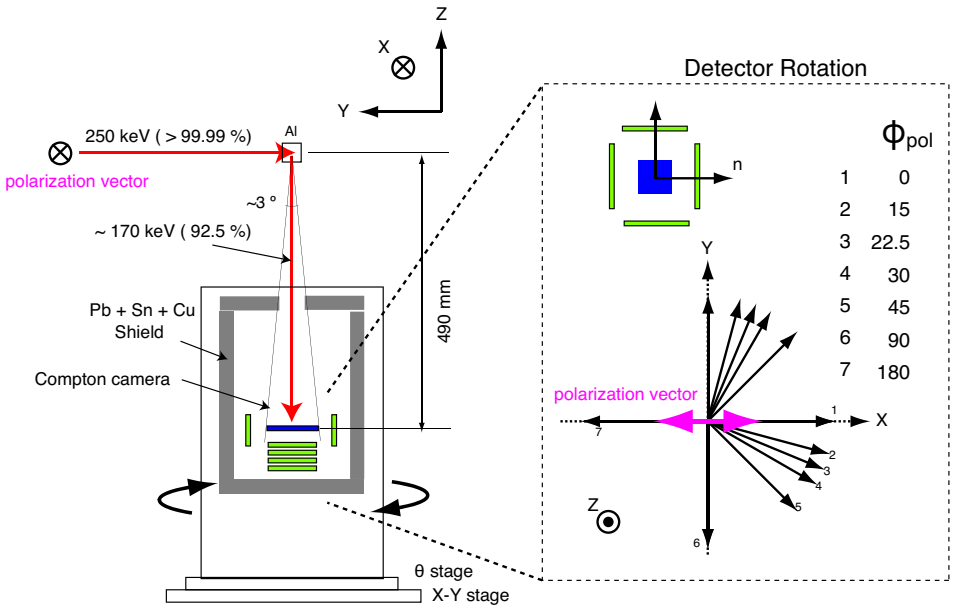

Fig. 5. Schematic view of experimental setup at beam line

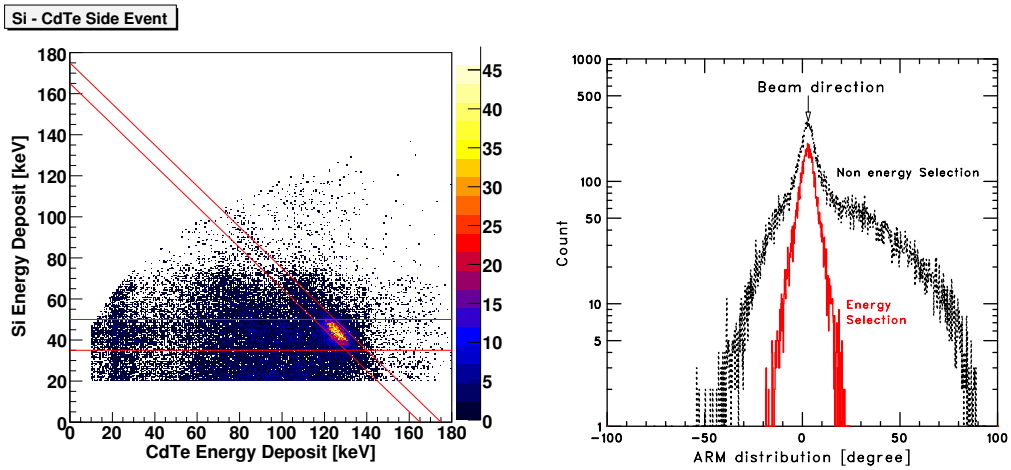

(a) (b)

Fig. 6. (a) Two-dimensional scatter plot of energy deposited in the DSSD and CdTe side detector. We used the events enclosed by the four straight lines for analysis. See the text for details. (b) ARM distribution before (dotted line) and after energy selection (solid line)

scattering angle distribution–$N_{\rm obs}(\phi)$–without any correction of detector response for the polarization angle $\phi_{\rm pol} = 0°$ (see Fig. 5). The experimental data (in the histogram) are compared with the simulation results (open square) for incident γ-rays with energy of 170 keV and 92.5% polarization. The counts around $-90°$ and $+90°$ are much higher than those around $0°$ and $180°$ due to the polarization of incident γ rays. The simulation reproduced features of the experimental data very well, including about 10% difference in counts between $-90°$ and $+90°$ resulting from the asymmetry of passive materials around the DSSD.

In order to make correction for detector response in the experimental results, we simulated $N_{\rm iso}(\phi)$ – the azimuth scattering angle distribution for non-polarized γ-rays–with energy of 170 keV, and compared with experimental data as shown in the bottom panel of Fig. 7. Note that, in the beam line setup, we could not obtain experimental data for

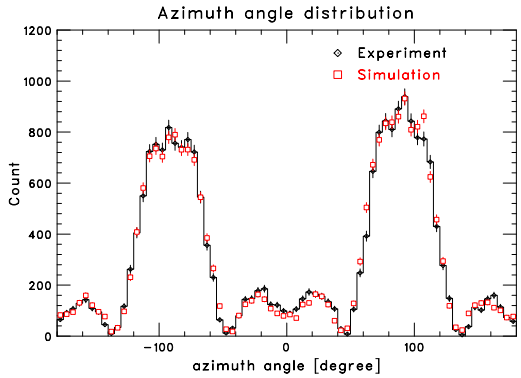

(a)

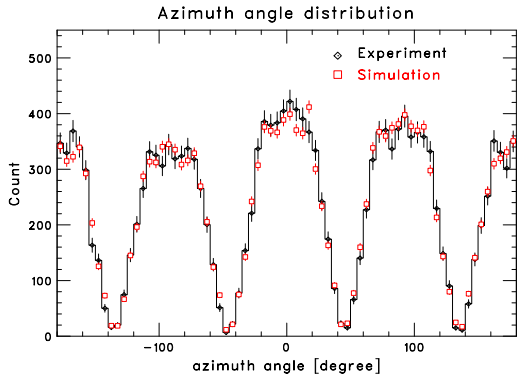

(b)

Fig. 7. Comparison of azimuth angle distribution between the experiment and simulation, (a) for polarized γ-rays and (b) for non-polarized γ rays. The simulated plot is normalized by the total integration of experimental counts.

non-polarized γ-rays directly. Instead, we obrained the response for non-polarized γ-rays by combining the data for the polarized vector of 0° and 90°. The polarization is cancelled by this procedure. In the simulation, we irradiated the DSSD with a non-polarized parallel beam 30 mm in diameter that corresponds to the dispersion of experimental incident γ rays. The gaps around $-135°$, $-45°$, 45° and 135° correspond to the absence of side CdTe detectors. When we did not consider any systematic error in the simulated $N_{\rm iso}(\phi)$, χ^2/ndf between experiment and simulation was an unacceptable value of 93.5/72. Reasonable χ^2/ndf of 62.3/72 was obtained, including 3% level systematic error. Therefore, we add 3% systematic error into $N_{\rm iso}(\phi)$ in addition to the statistical error of each point to account for simulator uncertainties in following analysis.

According to Equation 2, we obtained the azimuth angle distribution corrected for the detector response, $N_{\rm cor}(\phi)$, and derived the polarization parameters by fitting this distribution with the theoretical function of Equation 4 as shown in the bottom panel of Fig. 8. Note that we ignored the angle bins of $-135°\pm10°$, $-45°\pm10°$, $45°\pm10°$ and $135°\pm10°$, where the coverage by the side CdTe detectors is poor. Figure 9 summarizes $N_{\rm cor}(\phi)$ distribution for all experimental setups.

The fitting results for various experimental conditions are summarized in Table 2. The modulation factors were determined to be in the range of 0.82 to 0.85, with errors of 0.01 to 0.02. The modulation factor for 100% polarization at 170 keV (denoted by Q_{100}) was obtained as 0.925 ± 0.03 from the simulation. From Equation 6, the degree of polarization of the experimental incident beam is determined to be 89.7 ± 3.6%, which is consistent with the 92.5% incident degree of polarization expected for our experimental setup. The directions of the polarization vectors were determined for all measurements within accuracy of one degree. It should be noted that both the degree of polarization and direction of a polarization vector can be well determined even in an unfavorable polarization vector direction (e.g., $\phi_{\rm pol}$=45°), where the distribution of the azimuth scattering angle peaks in that direction correspond to gaps in the detector system.

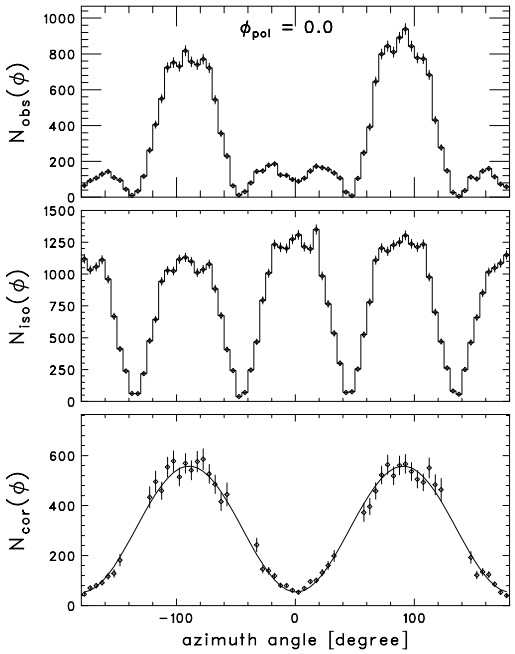

Fig. 8. (Top) $N_{\rm obs}(\phi)$ distribution (same as shown in Fig. 7) , (Middle) $N_{\rm iso}(\phi)$ distribution obtained by MC simulation, (Bottom) $N_{\rm cor}(\phi)$ with best fitted theoretical function.

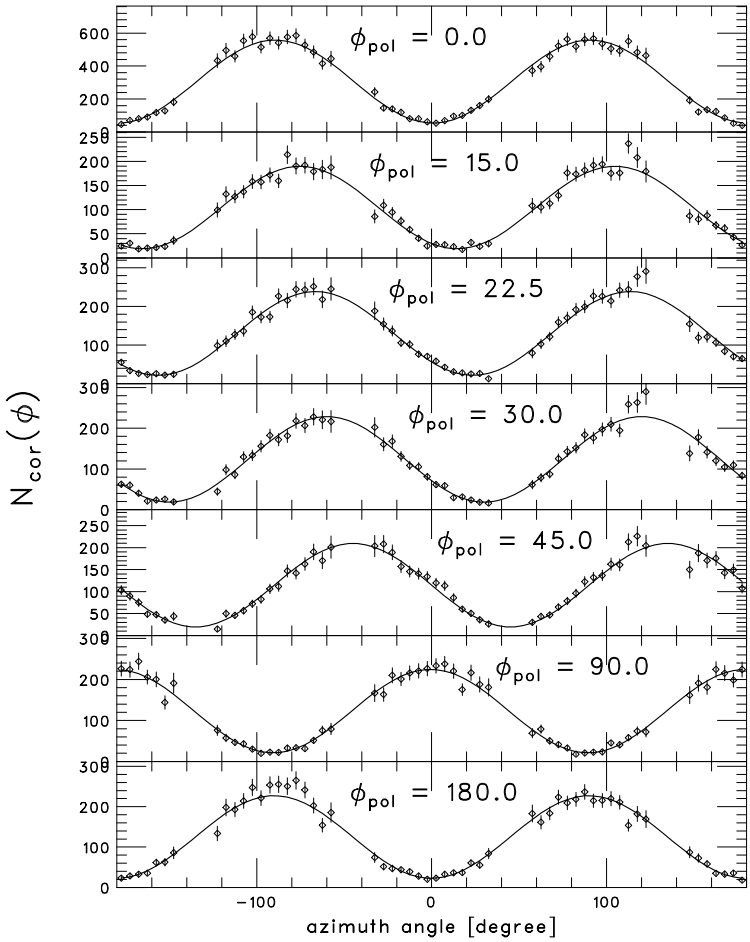

Fig. 9. Corrected azimuth angle distributions with fit curves for all experimental setups with different polarization angles.

	Modulation factor	Polarization vector	χ^2/ndf
Setup 1 ($\phi_{\rm pol} = 0.0$)	0.82 ± 0.01	0.6 ± 0.5	66.4/53
Setup 2 ($\phi_{\rm pol} = 15.0$)	0.82 ± 0.01	14.7 ± 0.7	56.0/53
Setup 3 ($\phi_{\rm pol} = 22.5$)	0.83 ± 0.01	23.4 ± 0.6	48.0/53
Setup 4 ($\phi_{\rm pol} = 30.0$)	0.85 ± 0.01	30.0 ± 0.6	52.8/53
Setup 5 ($\phi_{\rm pol} = 45.0$)	0.83 ± 0.02	45.0 ± 0.5	52.6/53
Setup 6 ($\phi_{\rm pol} = 90.0$)	0.83 ± 0.01	89.3 ± 0.6	44.5/53
Setup 7 ($\phi_{\rm pol} = 180.0$)	0.82 ± 0.01	180.1 ± 0.6	59.4/53

Table 2
Fit results for polarization parameters for all experimental setups with different polarization angles.

	Energy Range	Analyzing power	Efficiency	Area (cm^2)	Background (counts/sec)
SGD	80–300 keV	0.58	8.7 %	210	$\sim 1\times10^{-2}$

Table 3
Key polarimetric characteristics of the SGD.

7. SGD Polarimetric Performance

By building on the progress being made in advanced semiconductor detector and readout technologies, we are developing a semiconductor Compton camera for astrophysics applications in future satellite missions. Figure 10 shows the conceptual design of the Soft Gamma-ray Detector (SGD) for the ASTRO-H mission–the sixth Japanese X-ray satellite scheduled for launch in 2014. This Compton camera consists of stacked Si detectors surrounded by CdTe detectors, and is to be mounted inside the bottom of a well-type active BGO ($Bi_4Ge_3O_{12}$) shield in the detector unit of SGD. We adopted the concept of "narrow FOV (Field of View)" Compton camera in the SGD where the direction of the incident photons is constrained by the active shield and additional copper collimators. In this concept, we can eliminate backgrounds if the the direction of incoming photons calculated from the Compton kinematics is not consistent with the FOV. This background rejection technique can drastically reduce backgrounds due to the nuclear activation of detector materials and albedo neutrons, which are dominant backgrounds in the HXD (Hard X-ray Detector) [34,35], a predecessor of the SGD, onboard the Suzaku satellite [36].

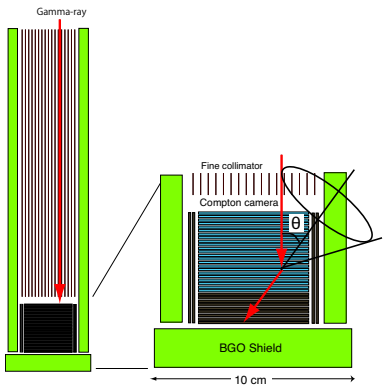

Fig. 10. Conceptual design of the Soft Gamma-ray Detector (SGD). Modules are arrayed to provide the required detection area for the ASTRO-H mission [18].

Based on recent detector designs, we calculated the key polarimetric characteristics of the SGD in the 80 to 300 keV band (Table 3). One SGD module consists of 32 central layers of Si detectors 0.6 mm thick, surrounded by eight layers of CdTe bottom detectors and two layers of CdTe side detectors 0.75 mm thick. A total of eight SGD modules are mounted on the ASTRO-H satellite. The background rate is calculated for orbit at an altitude of about 570 km and inclination of 32°, which is equivalent to the Suzaku's orbit. In-orbit data taken with the HXD-PIN Silicon detector onboard the Suzaku is used to estimate the flux of a non-X-ray background. According to recent studies [37], atmospheric neutrons are the major contributor to residual background in the HXD-PIN. For the SGD, this background is drastically reduced by employing requiring Compton kinematics. Based on data taken from experiments conducted at an accelerator [38], we added background due to activation caused by cosmic particles striking the CdTe detectors. The calculated SGD background is about two orders of magnitude lower than that of the HXD-PIN. More detailed studies on in-orbit performance are now being conducted.

The 3-σ minimum detectable polarization (MDP) [20] is calculated from effective area, analyzing power and estimated background rate (see Table 3). Figure 11 shows the estimated MDP with respect to observation time. Note that we did not take into account the systematic uncertainty from the detector-response function and asymmetries in backgrounds. These factors adversely affect the polarization sensitivity; therefore, improving the accuracy of response and precisely modeling the in-orbit background are both important. The SGD could realize MDP of 1.1% for 1 Crab sources and that of 3.6% for 100 mCrab sources after an observation time of 100 ksec.

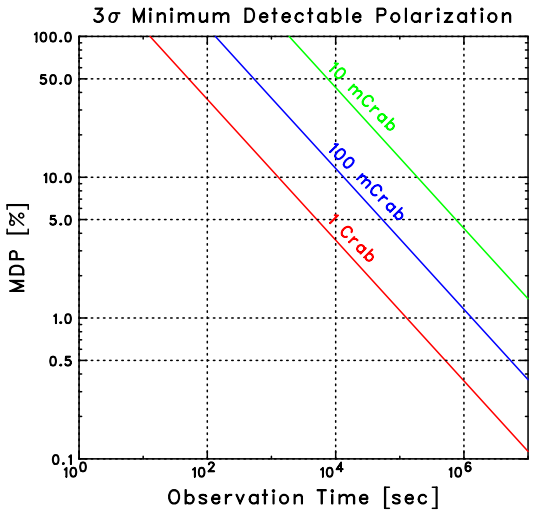

Fig. 11. Minimum Detectable Polarization (MDP) of the SGD in the 80 to 300 keV band for source brightnesses of 1, 1/10 and 1/100 of Crab as a function of observation time.

8. Summary

A prototype Compton camera consisting of a double-sided silicon strip detector and CdTe pixel detectors was developed, and the ability to measure polarization was demonstrated through a beam test. The direction of polarization vectors was determined to within an accuracy of one degree. For 168 keV incident γ-rays with 92.5% linear polarization, a modulation factor of 0.82 to 0.85 was obtained, which is consistent with the simulation results. We observed no strong systematic dependence of measured polarization properties on the polarization phase of the incident photon, in spite of the rotationally asymmetric configuration of the test set up, thanks to accurate simulation of the detector response.

The polarimetric performance of the SGD was estimated using a verified simulator in this study. Based on recent detector designs, the SGD could realize an MDP of 1.1% for a 1 Crab source and 3.6% for a 100 mCrab source after an observation time of 100 ksec. The capability of the SGD to measure polarization could afford a unique insight into the emission mechanism and geometrical structure of compact objects such as X-ray binaries or Active Galactic Nuclei.

References

[1] R. A. Sunyaev et al. Astron. Astrophys, Vol. 143, pp. 374-388, 1985
[2] A. K. Harding et al. Astrophys. J. Vol. 476, pp. 246-260, 1997
[3] P. Meszaros et al. Astrophys. J. Vol. 324, pp. 1056-1067, 1988
[4] T. Kamae et al. Astroparticle Physics, Vol. 30, Issue 2, pp. 72-84, 2008
[5] S. Gunji et al. Advances in Space Research 33, pp. 1771-1776, 2004
[6] N. Produit et al. Nucl. Instr. Meth. A., Vol. 550, pp. 616-625, 2005.
[7] E. Costa et al. Nature 411., pp. 662-665, 2001
[8] T. Takahashi et al. New Century of X-ray Astronomy, ASP, Vol. 251. pp. 210-213, 2002.
[9] T. Takahashi et al. SPIE, Vol. 4851, pp. 1228-1235, 2003.
[10] S. Watanabe et al. IEEE Trans. Nucl. Sci., Vol. 52, No. 5, pp. 2045-2051, 2005.
[11] S. Takeda et al. Proc. SPIE, Vol. 6706, 67060S 2007.
[12] S. Takeda et al. IEEE Trans. Nucl. Sci. Vol. 56, No. 3, pp. 783-790, 2009.
[13] R. Ribberfors. Phys. Rev. B, Vol. 12, pp. 2067-2074, 1975.
[14] T. Mitani et al., IEEE Trans. Nucl. Sci., Vol. 51, No. 5, pp. 2432-2437, 2004.
[15] H. Tajima et al. Proc. SPIE, Vol. 5488, pp. 561, 2004.
[16] http://www.spring8.or.jp/
[17] H. Tajima et al. IEEE Trans. Nucl. Sci., Vol. 52, pp. 2749-2757, 2005.
[18] T. Takahashi et al. Proc. SPIE, Vol. 7011, 70110O, 2008.
[19] http://astro-h.isas.jaxa.jp/
[20] F. Lei et al. Space Science Review, Vol. 82, pp.309-388, 1997.
[21] H. Tajima et al., in Proc. SPIE-Int. Soc. Opt. Eng., Vol. 4851, pp. 875-884, 2003.
[22] S. Takeda et al., Nucl. Instr. Meth. A., Vol. 579/2, pp. 859-865, 2007.
[23] SPIE newsroom http://spie.org/x20060.xml 2008.
[24] T. Takahashi et al. Proc. SPIE Vol. 3446, pp. 29-37, 1998.
[25] T. Takahashi et al. Nucl. Instr. Meth. A., Vol. 436, pp. 111-119, 1999.
[26] H. Tajima et al. IEEE Trans. Nucl. Sci., Vol. 51, pp. 842-847, 2004.
[27] T. Takahashi et al. 1st Space Wire Conference 2007.
[28] Z. He et al. Nucl. Instr. Meth. A., Vol. 463, pp. 250-267, 2001.
[29] A. Zumbiehl et al. Nucl. Instr. Meth. A., Vol. 469, pp. 227-239, 2001.
[30] A. Cola et al. Nucl. Instr. Meth. A., Vol. 568, pp. 406-411, 2006.
[31] J. Fink et al. Nucl. Instr. Meth. A., Vol. 560, pp. 435-443, 2006.
[32] G. Sato et al. Nucl. Instr. Meth. A., Vol. 541, pp. 372-384, 2005.
[33] G. Sato et al. IEEE Trans. Nucl. Sci., Vol. 49, No. 3, pp. 1258-1263, 2002.
[34] T. Kamae et al. Proc. SPIE, Vol. 2806, 314, 1996.
[35] M. Kokubun et al. IEEE Trans. Nucl. Sci., Vol. 51, pp. 1991, 2004.
[36] K. Mitsuda et al. Publ. Astro. Soc. Japan 58, SP1, S1–S8, 2007.
[37] T. Kitaguchi. Ph. D Thesis, The University of Tokyo, 2009.
[38] M. Murakami et al. IEEE Trans. Nucl. Sci., Vol.50, No.4, pp. 1013-1019, 2003.